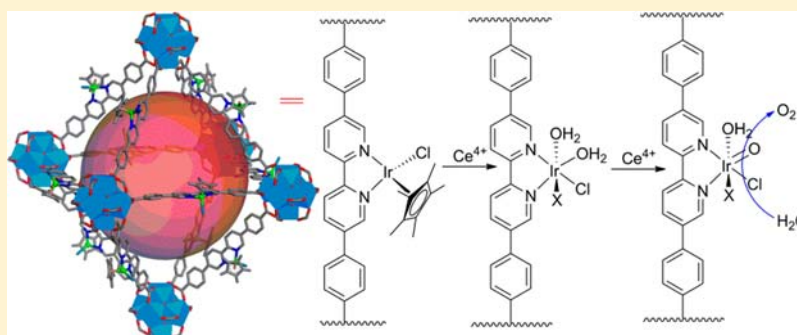# Elucidating Molecular Iridium Water Oxidation Catalysts Using Metal−Organic Frameworks: A Comprehensive Structural, Catalytic, Spectroscopic, and Kinetic Study

Cheng Wang,[†] Jin-Liang Wang,[†] and Wenbin Lin*

Department of Chemistry, CB #3290, University of North Carolina, Chapel Hill, North Carolina 27599, United States

S *Supporting Information*

ABSTRACT: As a new class of porous, crystalline, molecular materials, metal−organic frameworks (MOFs) have shown great promise as recyclable and reusable single-site solid catalysts. Periodic order and site isolation of the catalytic struts in MOFs facilitate the studies of their activities and reaction mechanisms. Herein we report the construction of two highly stable MOFs (**1** and **2**) using elongated dicarboxylate bridging ligands derived from Cp*Ir(**L**)Cl complexes (**L** = dibenzoate-substituted 2,2′-bipyridine, **bpy-dc**, or dibenzoate-substituted 2-phenylpyridine, **ppy-dc**) and $Zr_6O_4(OH)_4(carboxylate)_{12}$ cuboctahedral secondary building units (SBUs) and the elucidation of water oxidation pathways of the Cp*Ir(**L**)Cl catalysts using these MOFs. We carried out detailed kinetic studies of Ce^{4+}-driven water oxidation reactions (WORs) catalyzed by the MOFs using UV−vis spectroscopy, phosphorescent oxygen detection, and gas chromatographic analysis. These results confirmed not only water oxidation activity of the MOFs but also indicated oxidative degradation of the Cp* rings during the WOR. The (**bpy-dc**)Ir(H_2O)_2XCl (X is likely a formate or acetate group) complex resulted from the oxidative degradation process was identified as a competent catalyst responsible for the water oxidation activity of **1**. Further characterization of the MOFs recovered from WORs using X-ray photoelectron, diffuse-reflectance UV−vis absorption, luminescence, and infrared spectroscopies supported the identity of (**bpy-dc**)Ir(H_2O)_2XCl as an active water oxidation catalyst. Kinetics of MOF-catalyzed WORs were monitored by Ce^{4+} consumptions and fitted with a reaction−diffusion model, revealing an intricate relationship between reaction and diffusion rates. Our work underscores the opportunity in using MOFs as well-defined single-site solid catalytic systems to reveal mechanistic details that are difficult to obtain for their homogeneous counterparts.

1. INTRODUCTION

The oxidation of water to oxygen is the key half-reaction in both natural photosynthesis and the proposed water splitting scheme for solar energy harvesting/storage.[1] Considerable progress has been made on developing water oxidation catalysts (WOCs) over the past few decades. For example, a number of metal oxides, metal nitrides, and other metal salts have been shown by Domen, Nocera, Mallouk, Frei, and others as efficient catalysts to perform water oxidation both electrochemically and photochemically.[2] Compared to inorganic solid catalysts, molecular catalysts are more amenable to mechanistic studies and fine-tuning using synthetic chemistry to optimize their performances. Following the pioneering work of Meyer and co-workers on water oxidation reaction (WOR) with the Ru-based blue dimer,[3] molecules containing a variety of transition metals

(Ru, Ir, Mn, Fe, Co, Cu) have been identified as WOCs in recent years.[4,5]

Crabtree, Brudvig, and co-workers have extensively studied half-sandwich Cp*Ir complexes (Cp* is the pentamethylcyclo-pentadienyl ligand) as potential molecular WOCs.[6] However, due to the high-oxidation power of catalytic intermediates generated in the water oxidation process, at least some of these catalysts can undergo oxidative degradation during WORs.[6b,7] The ultimate decomposition products in Ce^{4+}-driven and electrochemically driven reactions were suggested to be iridium oxides/iridium hydroxides, which have been proven to be efficient WOCs.[2e,f,8] These observations raised concerns about

the molecular nature of the active catalysts based on the Cp*Ir complexes.

A number of elegant experiments have been performed by Crabtree, Brudvig, and co-workers as well as other research groups to elucidate the nature of the active catalytic species. $IrCl_3(H_2O)_3$ and $IrCl_6^{3-}$ were first ruled out by Crabtree, Brudvig, and co-workers to be the active catalysts, due to their insignificant water oxidation activity in the beginning stage of Ce^{4+}-driven reactions at pH = 1. IrO_2 nanoparticles were also not likely to be the active catalysts due to their drastically different kinetic isotope effect from Ir complexes when D_2O was used as the solvent.[6b] By carefully studying various Cp*Ir complexes as well as their CpIr analogs (Cp is the cyclopentadienyl ligand), Crabtree and co-workers showed that these compounds decomposed to varying degrees under the catalytic conditions (pH =1 and $[Ce^{4+}]$ = 78 mM).[9] For catalysts with only Cp* but no other chelating ligand, the complexes decomposed and formed nanoparticles under Ce^{4+}-driven reaction conditions[9] and a blue deposit on electrode under electrochemical conditions.[7a] The resultant nanoparticles/films from these reactions behaved similarly to iridium oxide/hydroxide but might contain organic residues. In contrast, Cp*Ir complexes with chelating ligands were stable at least during the beginning stage of the reaction.[6b] At longer reaction times, the activity of these catalysts decreased, but no nanoparticle formation in Ce^{4+}-driven reactions[9] or film formation during electrochemical catalysis[10] was unambiguously observed. The catalyst decomposition pathway was likely related to the oxidation of Cp* since the Cp analogs appeared to be more stable.[6b] Moreover, some of the catalysts that were previously reported to decompose to form nanoparticles with Ce^{4+} as the oxidant were found to remain molecular when IO_4^- was used as the oxidant.[11] The experimental evidence provided by Crabtree, Brudvig, and co-workers support that Cp*Ir complexes with chelating ligands are molecular catalysts.

Grotjahn and co-workers carried out comprehensive studies on the degradation of Cp*Ir complexes. They sequentially added Ce^{4+} to the catalyst solution and followed the generation of oxygen both in solution and in the gas phase.[7b] An induction period was observed before the detection of O_2 after the addition of the first <15 equiv of Ce^{4+} (initial $[Ce^{4+}]$ = 78 mM). This observation was interpreted as initial oxidation of the Cp* groups before water oxidation took place, which were supported by careful NMR and MS studies. They also provided some evidence for nanoparticle formation, but the TEM images and PXRD patterns were taken after the solvents were evaporated, which complicates the analysis because of crystallization of solution species. Their observation of an absorption peak in the 500−600 nm region, which was assigned as a signature absorption of IrO_x nanoparticles, can be alternatively explained by the formation of Ir(IV) molecular species, as pointed out by Crabtree and co-workers.[9] Macchioni and co-workers also performed detailed studies on the degradation pathway of Cp*Ir catalysts. By careful NMR studies, they found that oxidative degradation proceeds with an initial attack at the Cp* rings to form HCO_2H, CH_3CO_2H, and CH_2OHCO_2H.[7c,12] Fukuzumi and co-workers investigated the effects of bpy substituents on the stability of the Cp*Ir complexes in Ce^{4+}-driven water oxidation.[13] While the −OMe, −Me, and −CO_2H substituents at the 4,4′-positions of 2,2′-bipyridine (bpy) do not have a significant effect on catalyst degradation, the −OH groups at the 4,4′-positions of bpy significantly accelerate ligand decomposition. This substituent

effect was attributed to the oxidative susceptibility of the 4,4′-$(OH)_2$-bpy ligand.

The large body of experimental results indicates that the Cp* rings of these Ir complexes are easily oxidized during WORs, but it is likely that the active WOCs are molecular in nature. However, true identities of these molecular WOCs remain elusive to date, at least partly owing to the use of highly potent oxidants and the involvement of the complex $4e^-/4H^+$ process during WORs.

With the goal of building water splitting devices using molecular components, we became interested in using metal−organic frameworks (MOFs) and surface assemblies to study Cp*Ir-based WOCs. There are two distinct advantages in studying WOCs immobilized in MOF frameworks or on surfaces: (1) as the catalysts are isolated from each other in these assemblies, degradation pathways involving multiple molecules are prohibited, which greatly simplifies the mechanistic scenarios; (2) solid materials or surface-grafted moieties can easily be separated from solutions, which facilitates further characterization of the catalysts after WORs. We have previously grafted the $[Cp*Ir(bpy)Cl]^+$ and Cp*Ir(ppy)Cl (ppy is 2-phenylpyridine) catalysts onto the glassy carbon surface via diazonium coupling and studied their electrochemical water oxidation activities.[14] Although partially complicated by oxidation of glassy carbon electrode during catalysis, careful analyses of these immobilized complexes after WORs support the molecular nature of these catalysts.

Over the past decade, MOFs have emerged as a new family of crystalline and porous molecular materials that have shown great potential for many applications.[14−17] In particular, MOFs have provided a great platform to engineer single-site solid catalysts with tunable molecular functionalities, open channels, and other important attributes.[18] These MOF catalysts have enabled enhanced activities,[19] novel reactivities,[20] and unusual product selectivities.[21] We have recently reported water oxidation using MOFs that contain Cp*Ir catalysts. These MOFs were synthesized by doping Cp*Ir complexes with 5,5′-dicarboxylate-substituted bpy or ppy chelating ligands into the UiO-67 framework that is composed of $Zr_6O_4(OH)_4(carboxylate)_{12}$ SBUs and p-biphenyldicarboxylate bridging ligands.[22] The open channel sizes of those MOFs are however too small to allow hydrated Ce^{4+} ions to diffuse through, and consequently, only a minute fraction of the WOCs on the surfaces of these MOF particles is involved in water oxidation. It is of great interest to increase MOF channel sizes to allow all the catalytic struts to engage in water oxidation.

In this article, we report the synthesis and characterization of two new highly porous and stable Zr-carboxylate MOFs, **1** and **2**, built with elongated bpy or ppy ligands attached to the Cp*Ir moieties. We performed detailed kinetic studies of Ce^{4+}-driven WORs catalyzed by **1** and **2** using a combination of UV−vis spectroscopy, phosphorescent oxygen detection, and GC analysis. The recovered MOFs were then carefully studied for possible oxidative modification of the Cp* rings during WORs. After careful NMR and MS studies of the digested sample of **1**, (**bpy-dc**)Ir(H_2O)_2XCl (X is likely formic acid or acetic acid), formed by oxidative degradation of the Cp* rings, was identified as an active catalyst for water oxidation. The identity of the active WOC was further supported by X-ray photoelectron, diffuse-reflectance UV−vis absorption, luminescence, and infrared spectroscopies. With these mechanistic details in hand, a reaction−diffusion model was developed to describe the

Scheme 1. Chemical Structures of Homogeneous Control Catalysts and Synthesis of Zr-Carboxylate MOFs 1 and 2 of the fcu Topology
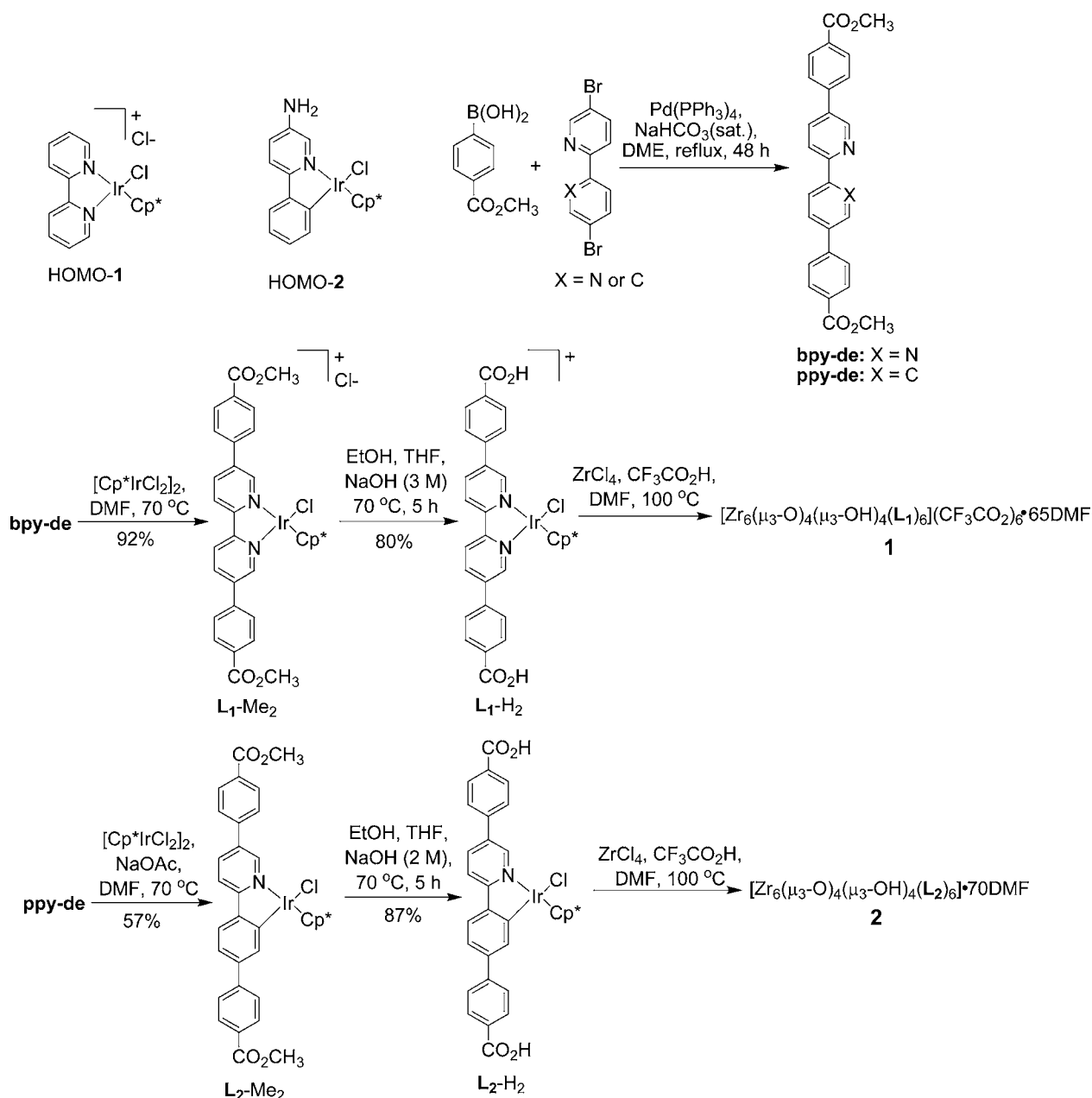
kinetics of MOF-catalyzed WORs. An understanding of the competition between reaction and diffusion rates provides important insights into these MOF-catalyzed WORs.

2. RESULTS AND DISCUSSION

2.1. Synthesis and Characterization of MOFs 1 and 2. The elongated dimethyl esters of 2,2′-bipyridine and 2-phenylpyridine (**bpy-de** and **ppy-de**) were prepared in high yields by Pd-catalyzed Suzuki coupling reactions between 4-(methoxycarbonyl)phenylboronic acid and 5,5′-dibromo-2,2′-pyridine or 5-bromo-2-(4-bromophenyl)pyridine, respectively. The corresponding dicarboxylic acids of **bpy-de** or **ppy-de** are denoted **bpy-dc** and **ppy-dc**, respectively. The dicarboxylic methyl ester-containing Ir complexes L_1-Me_2 and L_2-Me_2 were synthesized by treating [Cp*IrCl₂]₂ with **bpy-de** or **ppy-de** in DMF at 70 °C. L_1-Me_2 and L_2-Me_2 were isolated in 92% and

57% yields, respectively, and then converted to dicarboxylic acids L_1-H_2 or L_2-H_2 by base-catalyzed hydrolysis in 80% and 87% yield, respectively (Scheme 1). All of the new compounds were characterized by NMR spectroscopy and electrospray ionization-mass spectrometry [see Section S2, Supporting Information (SI)].

Highly stable MOFs **1** and **2** were synthesized by heating mixtures of L_1-H_2 or L_2-H_2 with ZrCl₄ and trifluoroacetic acid in DMF at 100 °C for 48 h. The resulting yellow crystalline solids were washed with copious amounts of DMF, methanol, and water. **1** and **2** were characterized by powder X-ray diffraction (PXRD), thermogravimetric analysis (TGA), scanning and transmission electron microscopy (SEM and TEM), X-ray photoelectron spectroscopy (XPS), and inductively coupled plasma-mass spectroscopy (ICP-MS). The crystals of **1** and **2** were not suitable for single-crystal X-ray diffraction
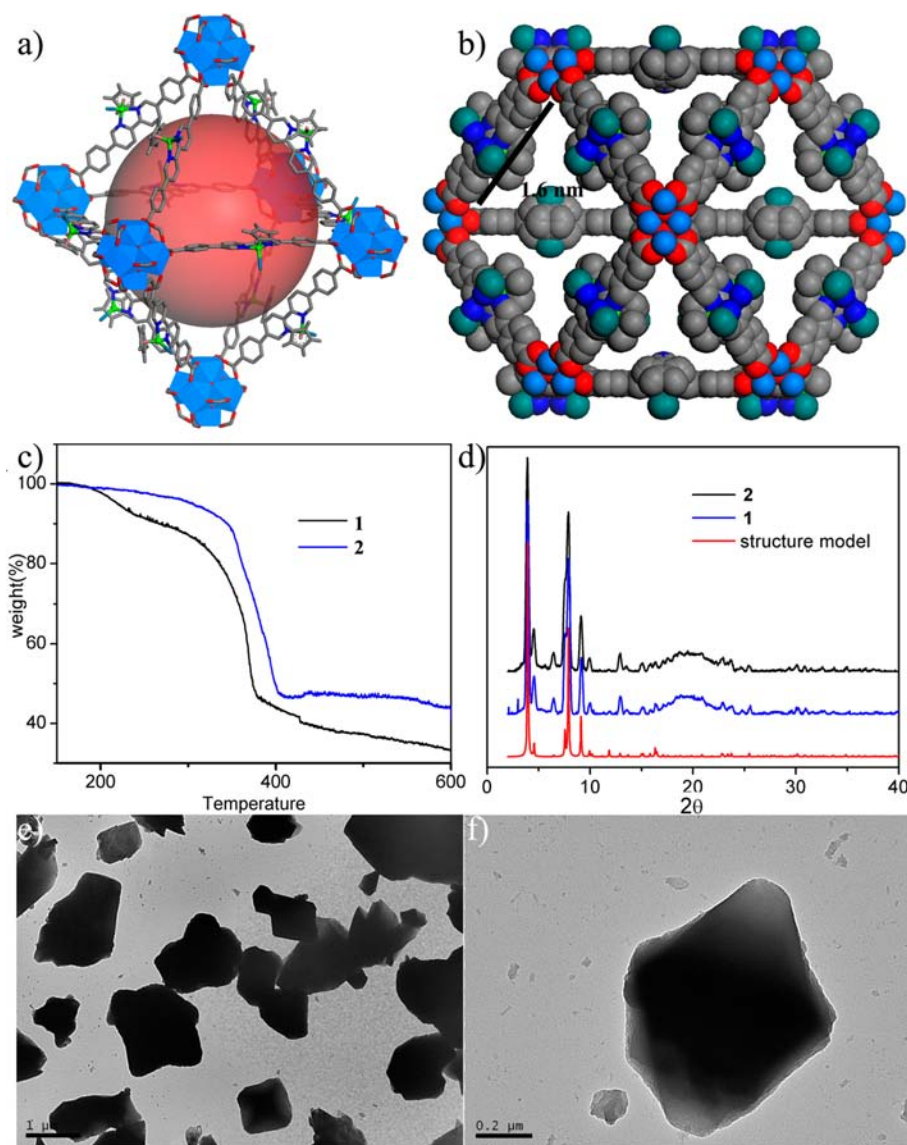
Figure 1. (a) Structure model for **1** showing an octahedral cage of 1 nm in diameter. Zr, blue polyhedron; Ir, green ball; Cl, dark green; C, gray; N, blue. The red ball in the middle represents the cage cavity. (b) Space-filling model of **1** as viewed along [110] direction. The triangular channel has an edge length of 1.6 nm. (c) TGA of solvent-free **1** (black) and **2** (blue). (d) PXRD patterns of **1** (blue) and **2** (black) along with the simulated PXRD pattern based on the structure model (red). TEM images of (e) microcrystals of **1** and (f) one microcrystal of **1** showing the octahedral shape.

analysis owing to their small sizes (in micrometers). Fortunately, as we expected, they are isostructural to the recently published UiO MOF with a similar bridging ligand (of the identical length to L_1 and L_2) based on the similarity of their PXRD patterns (Figure 1c).[23] **1** and **2** thus adopt the UiO framework structure of the **fcu** topology by connecting the $Zr_6(\mu_3\text{-O})_4(\mu_3\text{-OH})_4(\text{carboxylate})_{12}$ SBUs with the L_1 or L_2 linkers (Figure 1a). Because of the steric bulk of L_1 and L_2, **1** and **2** adopt noninterpenetrated structures, as confirmed by the systematic absences and relative peak intensities of their PXRD patterns (Section S3.4, SI). Based on PLATON calculations, **1** and **2** possess 66.0% and 69.5% of void spaces, respectively. Both **1** and **2** exhibit a triangular open channel with an edge length of 1.6 nm and an octahedral cavity with a diameter of 1 nm (Figure 1b).

SEM and TEM images of **1** showed octahedral microcrystals of ~1 μm in dimensions (Figures 1e,f and S5, SI), while SEM images of **2** showed aggregated microcrystals of 1−2 μm in

dimensions (Figure S6, SI). We used a combination of ^{1}H and ^{19}F NMR, TGA, and ICP-MS to establish the complete formulas of **1** and **2** to be $[Zr_6(\mu_3\text{-O})_4(\mu_3\text{-OH})_4(L_1)_6]$-$(CF_3CO_2)_6\cdot65DMF$ and $[Zr_6(\mu_3\text{-O})_4(\mu_3\text{-OH})_4(L_2)_6]\cdot70DMF$, respectively (Section S3.6, SI). The solvent contents of **1** and **2** are thus 35% and 40%, respectively. Freeze-dried samples of **1** exhibited negligible surface areas based on nitrogen adsorption measurements (Section S3.7, SI).[24] PXRD studies indicated severe framework distortion for **1** upon solvent removal (Section S3.7, SI), a phenomenon that has been observed for many MOFs with very large open channels.[15f,g,25] We also demonstrated the porosity of **1** by dye uptake measurements; **1** exhibited substantial amount (>20 wt %) of brilliant blue R-250 uptake (Section S3.6, SI).

2.2. Water Oxidation Activity of 1 and 2. We performed Ce^{4+}-driven WORs using **1** and **2** as catalysts. The WORs were studied by three different methods: (1) using a phosphorescent
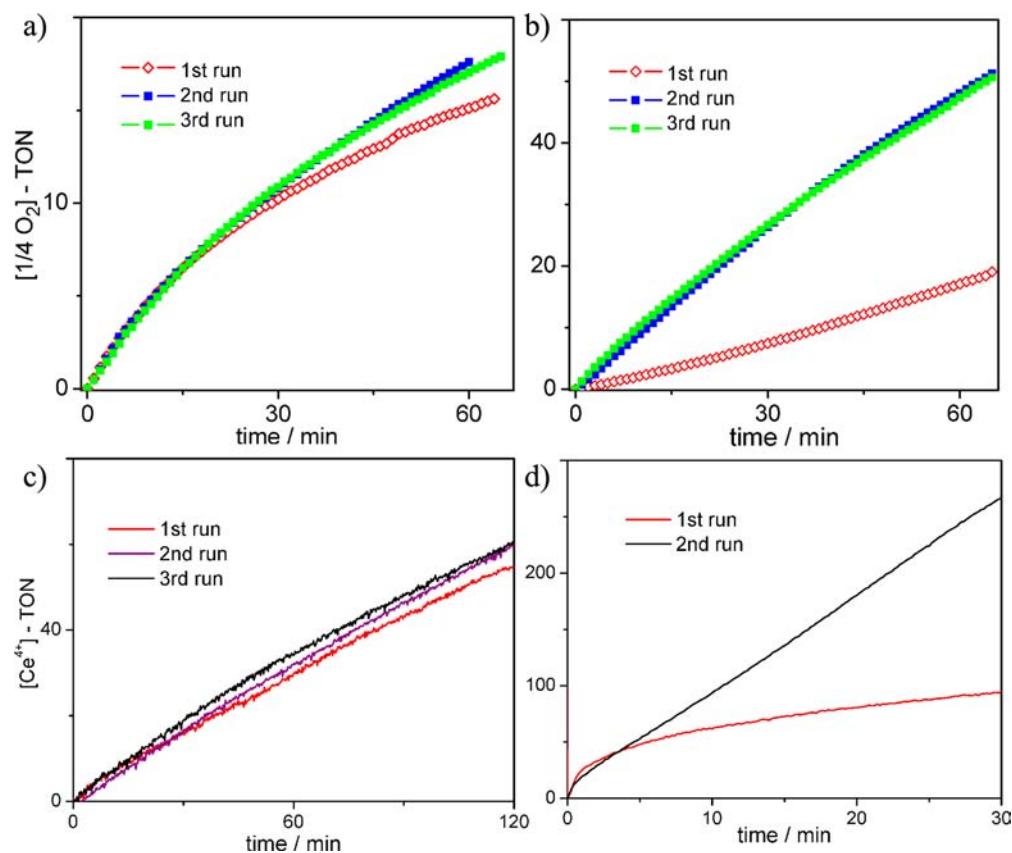
Figure 2. (a) Plots of O_2 evolving turnover number ($1/4$ O_2 TON) vs time for **1**. (b) Plots of O_2 evolving turnover number ($1/4$ O_2 TON) vs time for **2**. (c) Plots of Ce^{4+} consumption turnover number ($1/4$ O_2 TON) vs time for **1**. (d) Plots of Ce^{4+} consumption turnover number ($1/4$ O_2 TON) vs time for **2**. Experimental conditions: 3 mM Ce^{4+} in pH = 1 HNO_3 solution with 10 μM Ir.

oxygen sensor to detect the amount of O_2 in solution; (2) using UV−vis absorption at 420 nm to monitor Ce^{4+} consumptions; and (3) using gas chromatography (GC) to analyze the gas compositions in the headspace. The experiments were performed with 10 μM MOFs based on Ir in aqueous solutions of HNO_3 with pH = 1. The initial $[Ce^{4+}]$ was 3 mM for the WORs catalyzed by **1**.

As shown in Figure 2a, by quantifying the time-dependent oxygen generation using a phosphorescent sensor, a water oxidation turnover frequency (TOF) of 0.48 ± 0.02 min^{-1} (based on $1/4$ O_2 or 1 e^-) was obtained for **1** during the first 10 min of WOR (Table 1). At later time points, the oxygen generation appeared to slow down, owing to the formation of

Table 1. TOFs[a] of WORs Catalyzed by 1 and 2

	1 (min^{-1})	**2** (min^{-1})
UV−vis[b] (1st run)	0.52 ± 0.06	6.3 ± 1.0
UV−vis[b] (2nd run)	0.54 ± 0.07	9.4 ± 2.0
UV−vis[b] (3rd run)	0.53 ± 0.07	−
O_2 detection[b] (1st run)	0.48 ± 0.02	0.21 ± 0.02
O_2 detection[b] (2nd run)	0.48 ± 0.02	0.92 ± 0.05
O_2 detection[b] (3rd run)	0.47 ± 0.02	1.01 ± 0.05
GC detection	[c]0.40 ± 0.06	[d]1.7 ± 0.4

[a]TOF is based on $1/4$ O_2 or 1 Ce^{4+} (in other words, 1 e^-). [b]3 mM Ce^{4+} in pH =1 HNO_3 solution with 10 μM Ir, based on data from the first 10 min. [c]3 mM Ce^{4+} in pH = 1 HNO_3 solution with 10 μM Ir, based on data after reaction of 4 h. [d]3 mM Ce^{4+} in pH = 1 HNO_3 solution with 10 μM Ir, based on data after reaction of 2.5 h.

oxygen bubbles but not because of the deceleration of the WOR. The formation of oxygen bubbles reduced the percentage of generated O_2 that was detected by the phosphorescent sensor and caused significant fluctuations in the O_2 generation curves (Figures S10−S15, SI).

By monitoring the absorption peak intensity at 420 nm, the Ce^{4+} consumption rate was determined to be 0.52 ± 0.06 min^{-1} for **1** in the first 10 min of WOR (Figure 2c and Table 1). Comparisons of oxygen evolution rates determined by the phosphorescent sensor (0.48 ± 0.02 min^{-1}) to the Ce^{4+} consumption rates (0.52 ± 0.06 min^{-1}) gave an O_2 generation efficiency of >90% in the first 10 min of WORs. Since only 16 equiv of Ce^{4+} are needed to oxidize each coordinated Cp* group to 5 equiv of acetic acid, an O_2 generation efficiency of at least 94.7% would have been expected for a WOR with a total turnover number of 300 (based on the amount of Ir). Given the typical experimental errors (of several percents) for these measurements, the O_2 generation efficiency is thus not a sensitive indicator for ligand oxidation.

The headspace gas of the **1**-catalyzed WOR was also analyzed by GC to quantify the amount of O_2 generated from the WOR (Figures S16−S18, SI). The amount of CO_2 detected in the gas phase after water oxidation was not significantly different from the background signal (Figure S18, SI). The O_2 generation TOF was calculated by analyzing the headspace during the first 4 h of the WOR to be 0.40 ± 0.06 min^{-1} (Table 1). This TOF is slightly smaller than those obtained during the first 10 min of WORs, which again can be attributed to the O_2 bubble formation at later times of WORs.
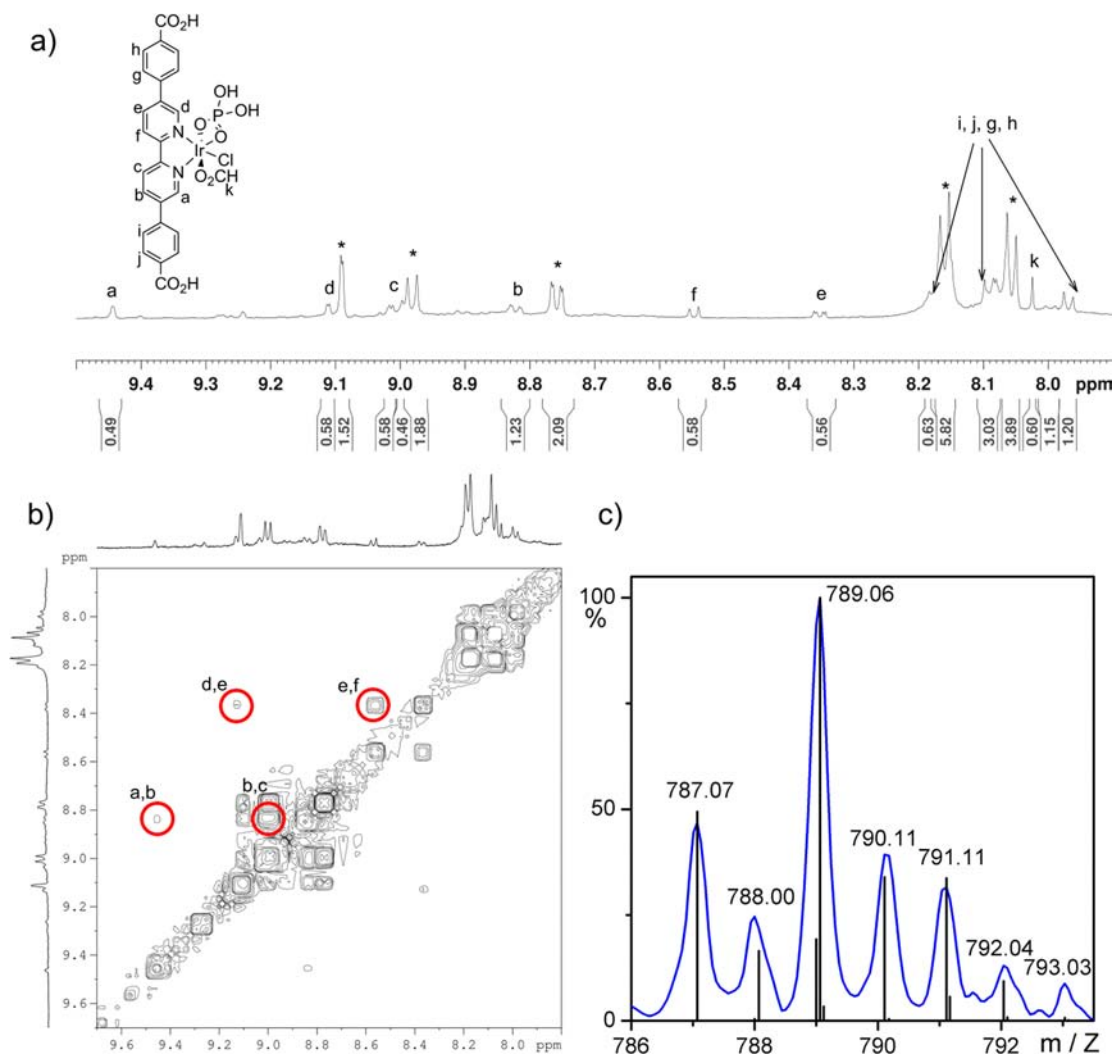
Figure 3. (a) ^{1}H NMR spectrum of digested **1** after WOR. A total of 30 equiv of Ce^{4+} were added successively to the pH = 1 HNO$_3$/D$_2$O solution with 1 mM Ir before the MOF is digested for NMR. Each time only 3 equiv of Ce^{4+} were added to give a [Ce^{4+}] of 3 mM. The next aliquot of Ce^{4+} is added after the complete consumption of the previous aliquot; * denotes peaks due to the original **L$_1$-H$_2$** ligand. Other major peaks are assigned to the proposed structure. (b) ^{1}H−^{1}H COSY spectrum of digested **1** after WOR. (c) ESI-MS of digested **1** (with phosphoric acid) after water oxidation showing the presence of the {[(**bpy-dc**)Ir(H$_2$PO$_4$)(HCO$_2$)Cl] + Na}$^+$ molecular ion. The black lines show the expected isotopic peaks.

To further examine the stability of the WOC derived from **1** under reaction conditions, we attempted to reuse **1** for water oxidation by adding fresh Ce^{4+} solutions to the recovered **1**. As shown in Figure 2a,c, **1** retained high catalytic activity for at least two consecutive reuses; the TOFs for the first and second reuse were slightly higher than that of the first use. Moreover, the supernatant from the reaction showed negligible water oxidation activity. ICP-MS analysis of the supernatant after water oxidation indicated that <1% of the Ir had leached into the solution. This is consistent with our assumption that at low [Ce^{4+}]'s, the active WOC derived from **1** is molecular in nature and does not dissociate from the MOF framework.

We also examined O$_2$ evolution from **2**-catalyzed water oxidation. PXRD and UV−vis studies indicated that the structure of **2** can be preserved at [Ce^{4+}] = 0.3 mM but will degrade quickly at higher [Ce^{4+}]'s. Unfortunately, we cannot accurately quantify oxygen at a [Ce^{4+}] of 0.3 mM due to the limited sensitivity of the oxygen sensor. The supernatants of the water oxidation mixtures with 0.3 mM Ce^{4+} contained less than 1% of Ir as revealed by ICP-MS studies. In an effort to confirm the water oxidation activity of **2**, we increased the [Ce^{4+}] to 3

mM, the same condition as that was used in the O$_2$ generation experiment for **1**. As shown in Figure 2b, **2** exhibited increasing O$_2$ generation rates with time. The initial O$_2$ generation TOF was 0.21 ± 0.02 min^{-1} (based on 1/4 O$_2$ or 1 e$^-$). Based on UV−vis measurements, a Ce^{4+} consumption rate was calculated to be 6.3 ± 1.0 min^{-1} for **2** in the first 10 min of WORs (Figure 2d). **2** thus has a 5% O$_2$ generation efficiency at the beginning state of WOR, with a significant amount of Ce^{4+} used for the oxidative degradation of **2**. We have also reused **2** as water oxidation catalyst twice after Ce^{4+} was depleted. The TOFs of second and third runs were significantly higher than that of the first run, indicating that the **2** decomposed to more active species during the WORs. Moreover, ∼6% of Ir was leached into the supernatants as revealed by ICP-MS studies. The drastically different behaviors of **1** and **2** under the same WOR conditions indicate that **2** is more prone to oxidative degradation than **1**, consistent with the fact that the electron-donating nature of the ppy chelator facilitates oxidative degradation of the ligand.

2.3. Identification of (bpy-dc)Ir(H$_2$O)$_2$XCl as an Active WOC in 1-Catalyzed Water Oxidation. As suggested by

other researchers in previous studies,[7b,c,12] significant modifications of the Cp* rings of the Cp*Ir catalysts occur during Ce^{4+}-driven WORs. In MOF-catalyzed WORs, multimolecular catalyst degradation pathways are shut down as a result of physical isolation of the catalytic struts. We thus believe that MOFs provide a unique platform to interrogate water oxidation pathways. In particular, we are interested in answering the following questions: (1) Do modifications of the Cp* rings happen in the catalytic struts of **1** during Ce^{4+}-driven WORs? (2) What is the chemical structure of the modified Ir compound? (3) Is the modified compound an active WOC? (4) Are large hydrated Ce^{4+} ions able to diffuse through the MOF channels to reach the active WOCs in the MOF interiors? (5) What roles do Ce^{4+} ion diffusion rates and water oxidation rates play in MOF-catalyzed WORs?

2.3.1. Identification and Quantification of Acetic Acid Generated from Oxidative Modifications of Cp Groups by* ^1H *NMR.* Oxidative degradation of the Cp* rings was previously shown to lead to the formation of acetic and formic acids and other decomposition products. Monitoring the reaction solution by ^1H NMR can thus provide information on the possible degradation of the Cp* rings on the Cp*Ir complexes. To afford an equivalent $[L_1]$ of 1 mM, 0.5 μmol of **1** was dispersed in 0.5 mL of D_2O, followed by successive addition of Ce^{4+}. Aliquots of 3 equiv of Ce^{4+} were added to the suspension each time, and ^1H NMR spectrum of the mixture was taken after complete consumption of the added Ce^{4+} in each cycle. Acetic acid and a small amount of formic acid were detected in the solution during the Ce^{4+}-driven WOR with **1**. The acetic and formic acid peaks in the NMR spectra were confirmed by spiking the solution with authentic samples. The amounts of acetic and formic acids generated from oxidative degradation of Cp* rings were quantified by integration of the ^1H NMR peaks with NMe_4^+ as an internal standard. The amount of generated acetic acid gradually increased after each addition of Ce^{4+} into the solution and plateaued at an amount around 1.8× of that of the total L_1 after adding 30 equiv of Ce^{4+} (Figure S19, SI). The amount of formic acid detected was <5% of that of L_1.

2.3.2. NMR and MS Studies of the Recovered 1 after WORs. To identify the active Ir catalysts after Cp* ring modifications, we characterized the digested sample of **1** after WORs by NMR and MS. The recovered solid was thoroughly washed with water before being dissolved in a 0.1 M D_3PO_4/d_6-DMSO solution. NMR spectra were taken on the dissolved samples with mesitylene as a standard. After treatment with 30 equiv of Ce^{4+}, 55% of the L_1 struts was oxidatively modified. Multiple modification products were observed in the ^1H NMR spectra, but the major modified species (28% of the original amount of L_1) was identified as $[(\mathbf{bpy\text{-}dc})Ir(solvent)_2XCl]^+$ based on the unsymmetrical **bpy-dc** coordination to the Ir center (Figure 3). The assignment of the proton signals was supported by the $^1H-^1H$ COSY spectrum. The X in the formula is likely to be a formate group resulting from the decomposition of the Cp* rings, as shown by a singlet at δ 8.02 in the ^1H NMR.[26]

The digested sample of **1** was also characterized by electrospray ionization-mass spectrometry (ESI-MS). The sample was digested either under acidic condition using 0.1 M H_3PO_4/DMSO or under basic condition using 0.1 M $NaOH/H_2O$, before being diluted with 1% formic acid/ methanol solution for ESI-MS measurements. For the sample digested with H_3PO_4, molecular ion peaks for $[(\mathbf{bpy\text{-}dc})Ir(H_2PO_4)(HCO_2)Cl]$ were observed ($[M + Na]^+$, expected:

789.00, observed: 789.06, Figure 3c). For the sample digested with NaOH, molecular ion peaks for $[(\mathbf{bpy\text{-}dc})Ir(H_2O)_2(HCO_2)Cl]^+$ were observed (M^+, expected: 705.06, observed: 705.14, Figure S20, SI). The assignments of these species are unambiguous because of the ^1H NMR spectroscopic data and the unique isotope patterns of the molecular ions in the mass spectra. We believe that $[(\mathbf{bpy\text{-}dc})Ir(H_2O)_2(HCO_2)Cl]^+$ is the most likely precatalyst in **1**-catalyzed WORs (Scheme 2). Presumably, $[(\mathbf{bpy\text{-}dc})Ir(H_2O)_2(HCO_2)Cl]^+$ is

Scheme 2. Oxidative Modifications of the Cp* Ring of the Catalytic Strut in 1 To Form (bpy-dc)Ir(H$_2$O)$_2$XCl and Proposed Oxidation of (bpy-dc)Ir(H$_2$O)$_2$XCl To Form the Ir(V)=O Species That Is Responsible for Water Oxidation
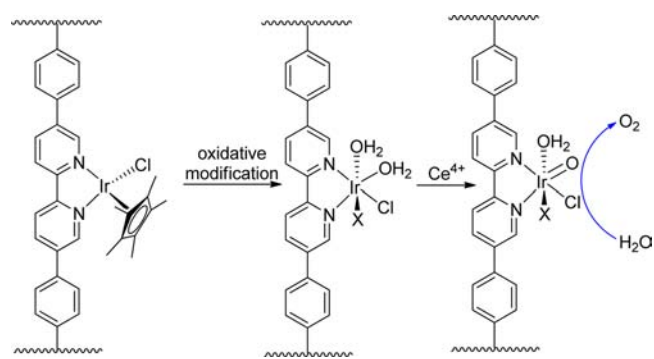
^{a}X is likely a formate or acetate ligand.

oxidized by Ce^{4+} via a proton-coupled electron transfer process to form the corresponding Ir(V)=O species (Scheme 2) which initiates the water oxidation catalytic cycle.

Although significant catalyst modification was observed for the MOF-catalyzed WORs, the O_2 generation curves did not show initial induction periods. This observation can be explained by the gradual modification of the L_1 ligand to the $[(\mathbf{bpy\text{-}dc})Ir(H_2O)_2XCl]^+$ species, which was supported by the slow increase of acetic acid upon the addition of Ce^{4+}. The lack of an initial induction period in the O_2 generation curve further implies that the original L_1 ligand in the MOF is also an active water oxidation with a comparable activity to that of the oxidatively modified one (i.e., the $[(\mathbf{bpy\text{-}dc})Ir(H_2O)_2XCl]^+$ species). Our experimental data however cannot unambiguously confirm this hypothesis.

2.3.3. Water Oxidation Activity of Soluble (bpy)Ir-(solvent)$_n$X$_m$ Species. To support the hypothesis that $(\mathbf{bpy\text{-}dc})Ir(H_2O)_2XCl$ is a true precatalyst for **1**-catalyzed WORs, we synthesized (bpy)Ir complexes containing water and chloride groups but no other ancillary ligands to test their water oxidation activities. Although $K[Ir(bpy)Cl_4]$ was not a competent WOC, its derivatives after treatment with $AgNO_3$ showed water oxidation activities with Ce^{4+} as the oxidant. Upon treating $K[Ir(bpy)Cl_4]$ with 4 equiv of $AgNO_3$ in pH = 1 (with added HNO_3), the resultant soluble species showed complicated ^1H NMR spectra, indicating the formation of multiple species due to incomplete Cl removal. Nevertheless, the resulting (bpy)Ir(solvent)$_n$X$_m$ mixture (with water and chloride or nitrate groups in addition to the bpy ligand, 25 μM based on Ir) was highly active for water oxidation in the presence of 10 mM Ce^{4+} at pH = 1. However, the water oxidation activity of this mixture decreased with time with an intractable dark-blue solid forming within 1 h (Figure S21, SI). The solid formation was due to aggregation of the Ir(IV) or
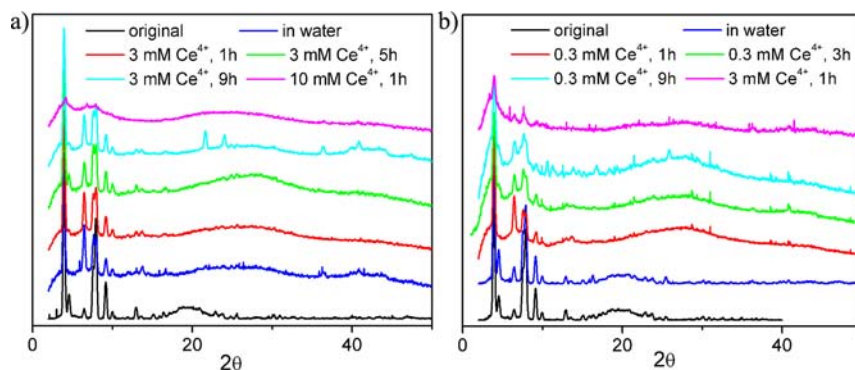
Figure 4. (a) PXRD patterns of **1** taken after different times of WORs. (b) PXRD patterns of **2** taken after different times of WORs. Experimental conditions: pH = 1 HNO$_3$ solution with 10 μM Ir at different Ce^{4+} concentrations and different reaction times.
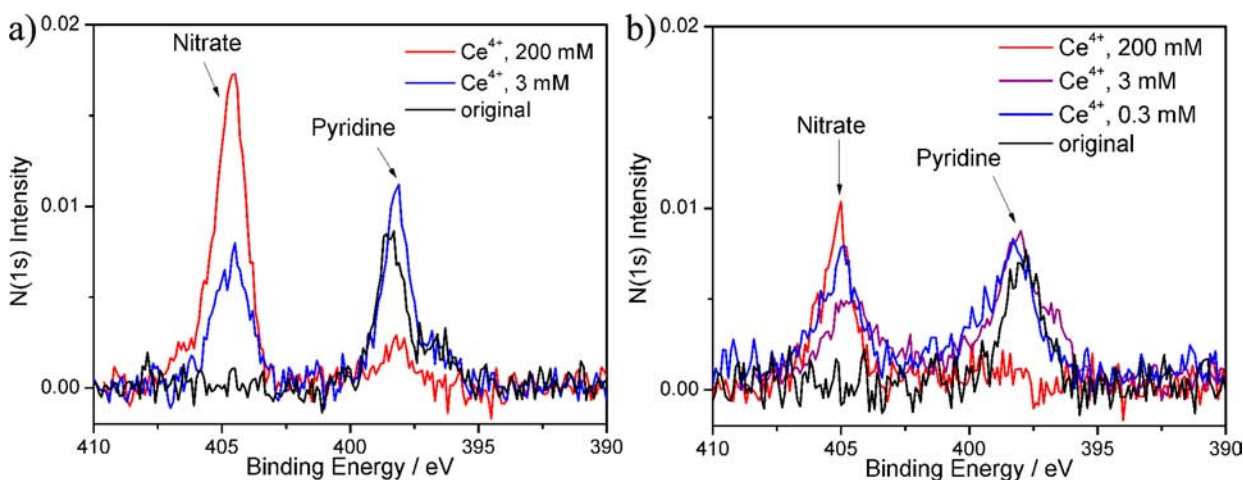

Figure 5. (a) N(1s) XPS signals for **1** after treatment with various [Ce^{4+}]'s at pH = 1 for 12 h: black, as-synthesized **1**; blue, after treatment with 3 mM Ce^{4+}; red, after treatment with 200 mM Ce^{4+}. (b) N(1s) XPS signals for **2** after treatment with various [Ce^{4+}]'s at pH = 1 for 12 h: black, as-synthesized **2**; blue, after treatment with 0.3 mM Ce^{4+}; purple, after treatment with 3 mM Ce^{4+}; red, after treatment with 200 mM Ce^{4+}. All the WOR experiments were done in pH = 1 HNO$_3$ solution with 10 μM Ir.

Ir(V) molecular species; such a process was prevented in the MOFs as a result of catalyst site isolation in the frameworks.

2.3.4. MOF Stability As Revealed by PXRD and ICP-MS Studies. PXRD studies indicated that the structure of **1** was preserved under WOR conditions (Figure 4). Since the oxidation of Cp* rings of the **L$_1$** ligands does not affect the MOF connectivity, the PXRD pattern is maintained even after the Cp* groups have been replaced with solvents and anionic ligands. The preservation of the PXRD patterns after WORs is thus consistent with the formation of the (**bpy-dc**)Ir-(H$_2$O)$_2$XCl species. ICP-MS measurements of the supernatant of the reaction mixture further confirmed the stability of **1** under the WOR conditions. After treatment of **1** with 3 mM Ce^{4+} at pH = 1 for 12 h, <1% of the Ir leached into the solution. In contrast, the framework of **2** can only be preserved at a [Ce^{4+}] of 0.3 mM. The framework structure of **2** is lost within 1 h of treatment with 3 mM Ce^{4+}, suggesting that the putative (**ppy-dc**)Ir(solvent)$_n$X$_m$ species further degrades to lead to even more active nonmolecular Ir water oxidation catalysts. Our attempts to isolate and identify the true precatalyst for **2**-catalyzed water oxidation have not yet been successful.

2.3.5. XPS Analyses of 1 and 2 before and after WORs. XPS analysis was performed on the recovered MOF solids (10 μM based on Ir) after treatment with various [Ce^{4+}]'s (0.3, 3, and 200 mM) at pH = 1 for 12 h. All the MOF samples were washed with nitric acid and dried on silicon wafer and then kept in vacuum overnight prior to XPS measurements. The spectra were calibrated with respect to the C(1s) peaks in each sample. The Ir(4f) region of the spectra showed no difference in peak positions between the original MOF and the samples treated with different [Ce^{4+}]'s, indicating the Ir(III) oxidation state in all of these samples (Figure S23, SI). We noticed that the MOFs remained in green color in a pH = 1 solution after all of the Ce^{4+} ions were consumed. The green color suggested the Ir(IV) oxidation state for the resting state of the catalysts at low pH. These MOFs however reverted to the original yellow-red color after treatment with neutral water (see Section 2.3.6). We believe that the observation of the Ir(III) oxidation state by XPS is due to the ready reduction of the recovered MOFs either during the drying and vacuum processing prior to XPS measurements or by X-rays or the generated photoelectrons during the XPS measurements. XPS thus cannot be considered a reliable technique for determining the oxidation states of Ir WOCs. The signal intensity of Ir(4f), N(1s), and Zr(3d) peaks all decreased with respect to the C(1s) peak intensity at increasing [Ce^{4+}]'s, presumably caused by adsorbed Ce^{4+} and NO$_3^-$ ions on the MOF surface. The XPS spectra also showed two different N(1s) peaks at binding energies of 398.2 and 404.6 eV for the pyridyl and nitrate nitrogen atoms, respectively (Figure 5). The atomic ratios of Ir vs pyridyl nitrogen in these
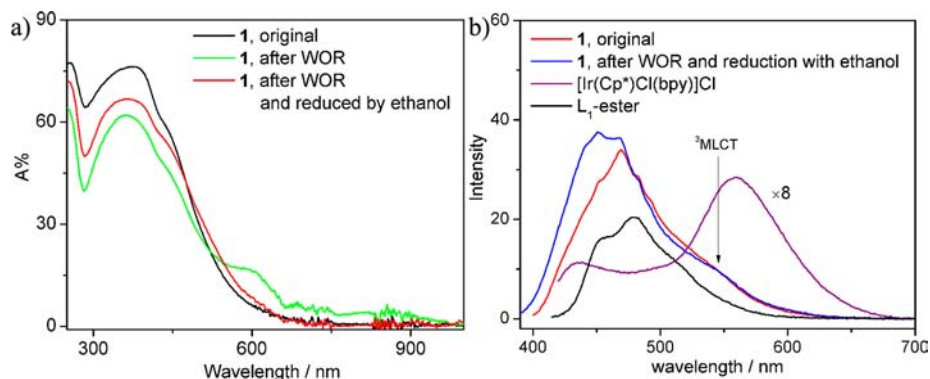
Figure 6. (a) Diffuse reflectance spectra of **1**: original (black), after WOR (green), and after WOR and then reduction with ethanol (red). (b) Fluorescence spectra of **1** before and after WORs. The spectra were taken with an acetonitrile suspension of MOFs with a [Ir] of 0.4 mM. The excitation wavelength was 370 nm, and no optical filter was used in the measurement. The L_1-Me$_2$ and [Ir(Cp*)Cl(bpy)]Cl were dissolved in acetonitrile with a [Ir] of 0.4 mM. WOR conditions: 3 mM Ce^{4+} in pH = 1 HNO$_3$ solution with 10 μM Ir.

samples provide useful information on the stability of chelating **bpy-dc** and **ppy-dc** ligands. As shown in Table S2, SI, the atomic ratios of Ir vs pyridyl nitrogen remained constant for both **1** and **2** after treatment with relatively low [Ce^{4+}]'s, suggesting that the Ir atom and pyridine moiety in **bpy-dc** and **ppy-dc** ligands remain intact under these conditions. However, under high [Ce^{4+}]'s, the atomic ratios of Ir vs pyridyl nitrogen decreased significantly compared to those of the original MOFs, suggesting loss of Ir from the MOFs as a result of partial degradation of the chelating ligands (see Section 2.4). It is noted that the deviation of Ir vs pyridyl nitrogen atomic ratios from the ideal atomic ratios is due to different electron collection efficiency for different elements in the samples, which is not uncommon for XPS analyses.

2.3.6. Diffuse Reflectance UV–vis Measurements of 1 after WORs. The recovered **1** after treatment with Ce^{4+} (3 mM) overnight was washed with copious amounts of 0.1 M HNO$_3$ solution. The recovered solid exhibits a green color, suggesting an Ir(IV) species as the catalyst resting state. Note that if the solid is washed with water (pH = 7), the green color will slowly change to the original yellow-red color, suggesting that the Ir(IV) species is not stable at neutral pH. Diffuse-reflectance UV–vis spectrum of the recovered **1** (after washing with 0.1 M HNO$_3$ solution) was taken by pressing the solids onto a smooth BaSO$_4$ surface. As shown in Figure 6a, an additional peak at ~600 nm appears in the solid when compared to **1**, corresponding to the Ir(IV) species at resting state.[9] Interestingly, the Ir(IV) species of the recovered **1** was readily reduced to Ir(III) species by adding a few drops of ethanol to the pressed solid sample (for diffuse reflectance UV–vis measurements). The spectrum taken after evaporation of ethanol lost the peak at ~600 nm, suggesting a complete reduction of the Ir(IV) species to Ir(III). This reversible oxidation/reduction of the Ir species is consistent with the molecular nature of water oxidation catalysts. The peak intensities of the diffuse reflectance spectra cannot be exactly reproduced in each measurement due to different sample positions and other experimental variables.

2.3.7. Luminescence Spectroscopy of 1 after WORs. [Cp*Ir(bpy)Cl]$^+$ and its derivatives are weakly luminescent in acetonitrile. Luminescence spectra can sensitively probe the Ir coordination environments. The recovered **1** was reduced to the Ir(III) oxidation state by washing with ethanol, and the luminescence spectra were taken with an acetonitrile suspension of the reduced MOF at a [Ir] of 0.4 mM. As

shown in Figure 6b, the shoulder peak at ~550 nm for **1** before and after WORs was assigned to emission from the triplet metal-to-ligand (^{3}MLCT) excited state of the Ir complexes by comparing with the emission spectra of the parent [Cp*Ir-(bpy)Cl]$^+$ complex. The presence of the MLCT emission band after WORs indicated that Ir is still coordinated to the bpy moiety in **1**. The strong emissions at shorter wavelength are due to the fluorescence of the **bpy-dc** ligand with vibrational fine structures, whereas the different intensities of different vibrational bands of the **bpy-dc** ligand for the samples before and after WORs can be accounted for by modifications of the Cp* ligand during the WOR.

2.4. [Ce^{4+}]-Dependent Degradation of MOF WOCs. The observed degradation of **2** at 3 mM of Ce^{4+} prompted us to carefully examine the degradation of MOF WOCs during WORs. The degradation of MOF WOCs can be inferred from the kinetic data of WORs, as determined by Ce^{4+} consumption rates using UV–vis spectroscopy. The catalyst decomposition rate is shown to be very sensitive to the [Ce^{4+}].

For **1**-catalyzed reactions, the kinetics of Ce^{4+} consumption becomes much faster when the [Ce^{4+}] exceeds 4.5 mM (Figure 7a), suggesting the decomposition of the MOF catalyst to form more active WOCs under these conditions. This decomposition kinetics can be more clearly visualized by plotting [Ce^{4+}]/C_0 vs t (C_0 is the initial concentration of Ce^{4+}) (Figures S28 and S29, SI). At C_0 < 4.5 mM, [Ce^{4+}]/C_0 decays more slowly as C_0 becomes higher. However, At C_0 > 4.5 mM, [Ce^{4+}]/C_0 decays faster as C_0 becomes higher. This [Ce^{4+}]-dependent behavior indicates that MOF decomposition has a high order dependence on [Ce^{4+}].

To further confirm this [Ce^{4+}]-dependent decomposition, the MOF after being treated with 9 mM Ce^{4+} was recovered after all of the Ce^{4+} ions were consumed and reused in a new run of water oxidation with 3 mM Ce^{4+}. The recovered MOF showed much faster Ce^{4+} consumption as shown in Figure 7c, supporting the decomposition of the MOF at high [Ce^{4+}]'s. To test if the decomposition is caused by the generated Ce^{3+}, a solution with 1.0 mM Ce^{4+} and 9 mM Ce^{3+} was used in a catalytic run. The added Ce^{3+} slowed the Ce^{4+} consumption rate, ruling out the possibility that Ce^{3+} caused decomposition of the MOF (Figure 7d). The slower Ce^{4+} consumption of the Ce^{3+}-added solution is due to slower Ce^{4+} diffusion at a higher total Ce concentration, which will be further discussed in Section 2.5.
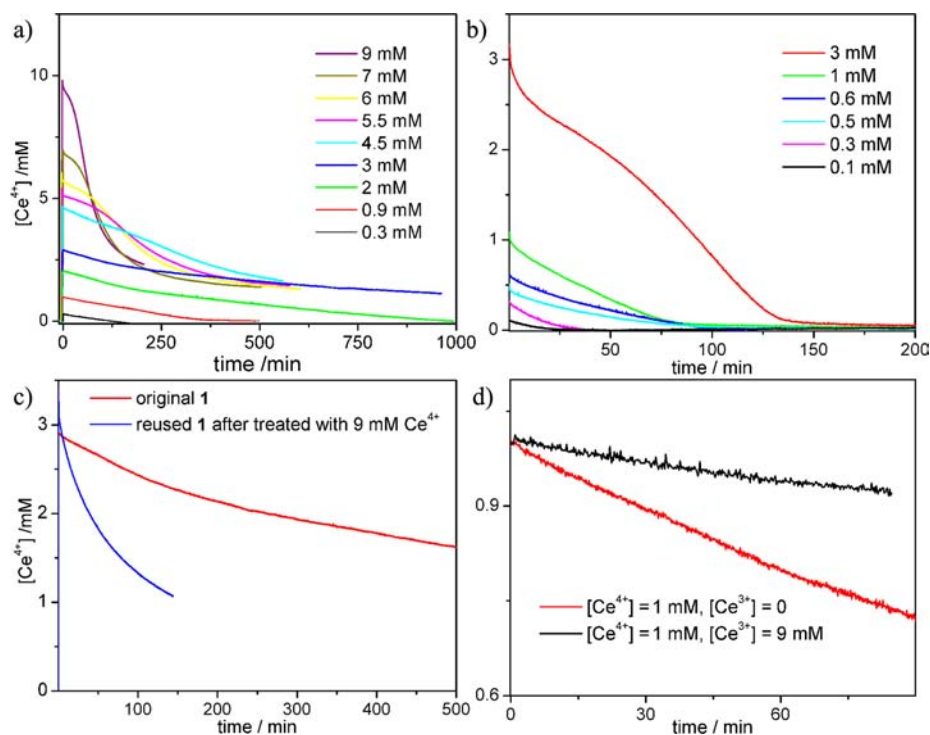
Figure 7. (a) $[Ce^{4+}]-t$ plots of **1**-catalyzed WORs under different initial $[Ce^{4+}]$'s. (b) $[Ce^{4+}]-t$ plots of **2**-catalyzed WORs under different initial $[Ce^{4+}]$'s. (c) $[Ce^{4+}]-t$ plots of **1**-catalyzed WORs with an initial $[Ce^{4+}]$ of 3 mM, before and after treatment with 9 mM Ce^{4+}. (d) $[Ce^{4+}]-t$ plots of **1** catalyzed-WORs with an initial $[Ce^{4+}]$ of 1.0 mM, in the presence and absence of 9 mM Ce^{3+}. All the WOR experiments were performed in pH = 1 HNO_3 solution with 10 μM Ir.

UV−vis data showed that **2** is more prone to decomposition than **1** (Figure 7b). At an initial $[Ce^{4+}]$ of 3 mM, **2** quickly decomposed as indicated by the Ce^{4+} consumption rate. The decomposition of **2** is further supported by the observation that at an initial $[Ce^{4+}]$ of 0.5−3 mM, the Ce^{4+} consumption rate was much higher for the second catalytic run than the first one (Figures S50−S55, SI).

MOF decomposition was also confirmed by PXRD studies. PXRD patterns of the MOFs were taken at different time points with different initial $[Ce^{4+}]$'s. The broadening or even disappearance of the PXRD peaks at high $[Ce^{4+}]$'s is indicative of framework decomposition. Moreover, there is strong correlation between UV−vis kinetics and PXRD patterns on the onset of MOF decomposition. At higher $[Ce^{4+}]$'s, the UV−vis data showed accelerated consumption of Ce^{4+} when the PXRD pattern indicated that MOFs started to decompose. It is likely that the Ir moieties are released into solution to form much more active nonmolecular WOCs when the MOF structures collapse, leading to much enhanced Ce^{4+} consumption rates.

To investigate if the MOF decomposition is due to the instability of the SBUs, we synthesized an analogous UiO MOF using the 5-benzoic-2-(4-benzoic-phenyl)-pyridine acid (**ppy-dc**) bridging ligand and $Zr_6O_4(OH)_4(carboxylate)_{12}$ SBUs. This Ir-free MOF exhibits the same UiO topology but adopts an interpenetrated structure as revealed by the systematic absence of the [200] peak in its PXRD pattern (Figure S22, SI). As shown by the PXRD patterns of the MOF after acid and Ce^{4+} treatment, the MOF is stable in pH = 1 water solution and is much more stable than **1** and **2** at high $[Ce^{4+}]$. This control experiment indicates that the UiO framework and SBUs are stable under WOR conditions. The decomposition observed for

1 and **2** at high $[Ce^{4+}]$'s is thus attributed to degradation of $\mathbf{L_1}$ and $\mathbf{L_2}$ moieties under these harsh conditions.

2.5. Diffusion Reaction Model for MOF-Catalyzed Water Oxidation. Little is known about kinetics of MOF-catalyzed reactions, due to the difficulty in following MOF-catalyzed reactions and complicated data analysis involving both reaction kinetics and reactant/product diffusion rates. In this Ce^{4+}-driven WOR, however, the reaction can be readily followed by UV−vis spectroscopy to accurately determine the consumption rate of Ce^{4+}. Kinetic analyses of MOF-catalyzed Ce^{4+}-driven WORs are further simplified due to two factors: (1) water is the reactant whose concentration remains constant throughout the WOR; and (2) the product, oxygen molecules, can diffuse quickly and does not require consideration.

Water oxidation experiments were performed at several different initial $[Ce^{4+}]$'s. The $[Ce^{4+}]$'s determined from UV−vis measurements were plotted against reaction time t. **1** and **2** exhibited different kinetic behaviors. For **1**, the $[Ce^{4+}]-t$ plot is linear at the initial stage, indicating a quasi-zeroth-order reaction with respect to $[Ce^{4+}]$. The deviation from a linear relationship at later times (particularly for higher $[Ce^{4+}]$'s) is likely due to the decomposition of MOF catalysts. This quasi-zeroth-order reaction rate depends on initial $[Ce^{4+}]$ (Figures 8a and S32−S40, SI). For **2**, the $\ln[Ce^{4+}] - t$ plot is linear at the initial stage, indicating a quasi-first-order reaction with respect to $[Ce^{4+}]$ (Figures 8b and S44−S49, SI). We will show below that these seemingly different kinetic behaviors can be explained using the same reaction−diffusion model with different Ce^{4+} diffusivities and WOR rates for **1** and **2**.

With $c(r,t)$ denoting the $[Ce^{4+}]$ inside a MOF (where r is the distance from the center of a spherical MOF particle and t is the reaction time), we can write eq 1 to express $c(r,t)$ by considering diffusion of Ce^{4+} inside a MOF particle following
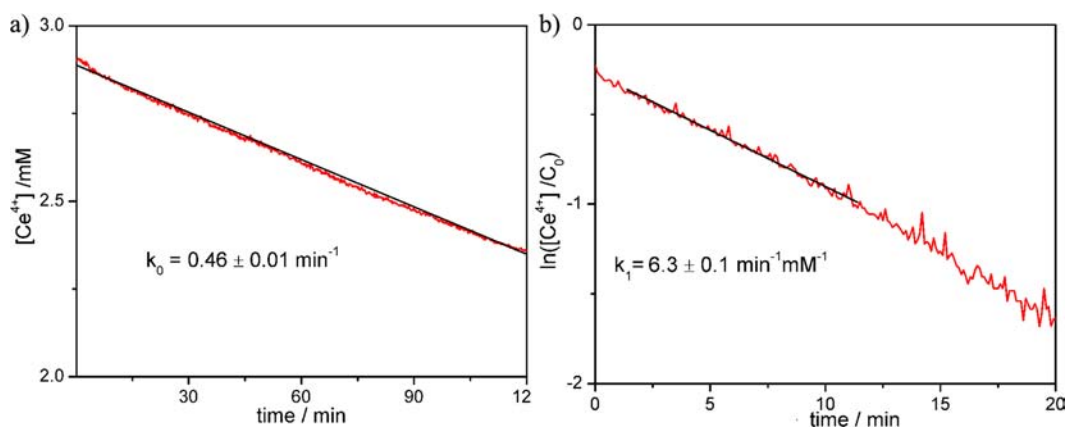
Figure 8. (a) $[Ce^{4+}]-t$ plot of **1**-catalyzed water oxidation. The initial $[Ce^{4+}] = 2.88$ mM. The linear curve indicates a quasi-zeroth-order reaction with respect to $[Ce^{4+}]$, leading to a rate constant of $k_0 = 0.46 \pm 0.01$ min^{-1}. (b) $\ln([Ce^{4+}]/C_0)-t$ plot of **2**-catalyzed water oxidation. The initial $[Ce^{4+}] = 0.32$ mM. The linear fitting indicates a quasi-first-order reaction with respect to $[Ce^{4+}]$, leading to a rate constant of $k_1 = 6.3 \pm 0.1$ min^{-1} mM^{-1}. All the WOR experiments were performed in pH = 1 HNO$_3$ solution with 10 μM Ir.
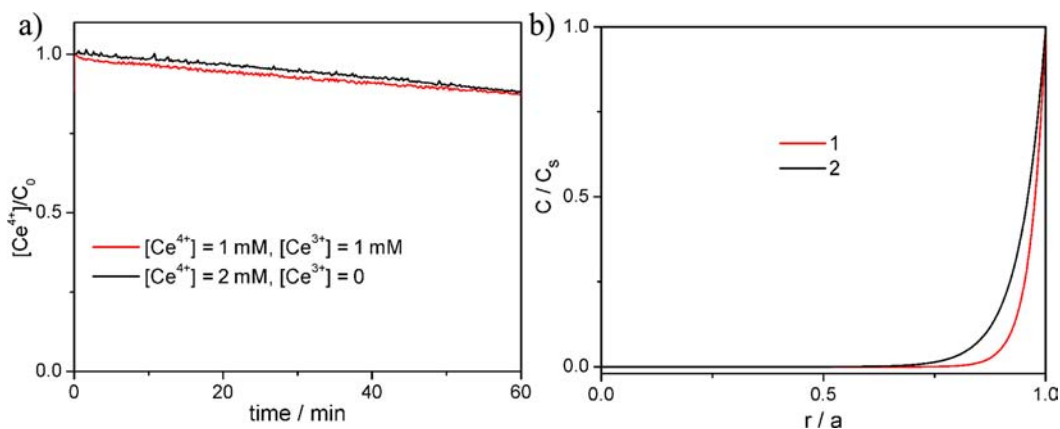

Figure 9. (a) Ce^{4+} consumption monitored by UV−vis spectroscopy at 420 nm for **1** with an initial $[Ce^{4+}]$ of 1 mM and a $[Ce^{3+}]$ of 1 mM (red) vs a $[Ce^{4+}]$ of 2 mM and a a $[Ce^{3+}]$ of 0 mM (black). The overlap of these two curves indicates similar influence of $[Ce^{4+}]$ and $[Ce^{3+}]$ on the diffusivity of Ce^{4+}. The experiments were performed in pH = 1 HNO$_3$ solution with 10 μM Ir. (b) Ce^{4+} distributions inside the particles of **1** and **2**. The initial $[Ce^{4+}]$ is 1 mM. C_s is the $[Ce^{4+}]$ in the solution.

Fick's law (the first term) and the WOR catalyzed by the isolated Ir sites with a first-order dependence on the local $[Ce^{4+}]$ (the second term). The corresponding boundary conditions to describe this reaction−diffusion process inside the MOF particle are shown in eqs 2 and 3:

$$\frac{\partial c(r,t)}{\partial t} = D\frac{1}{r^2}\frac{\partial}{\partial r}\left(r^2\frac{\partial c(r,t)}{\partial r}\right) - kc(r,t) \tag{1}$$

$$t = 0, \quad 0 < r < a, \quad c = 0; \quad r = a, \quad c = c_0 \tag{2}$$

$$r = a, \quad V\frac{\partial c(r,t)}{\partial t} = -N \cdot 4\pi a^2 D\frac{\partial c(r,t)}{\partial r} \tag{3}$$

where the radius of the MOF particle is a (the particle is approximated as spherical); the total solution volume is $V = 2$ mL; the MOF concentration (the concentration of ligand **L** in the solution) is $C_{MOF} = 10$ μM; the Avogadro's constant is $N_A = 6.02 \times 10^{23}$ mol^{-1}; the volume of unit cell per ligand **L** from the crystal structure is $v = 2.4$ nm^3; the number of MOF particles in the solution is $N = V \cdot C_{MOF} \cdot N_A \cdot v/(4/3\pi a^3)$; the diffusivity of Ce^{4+} inside MOF is D; the initial $[Ce^{4+}]$ in solution is C_0; and the rate constant of reaction inside MOF is k (first order with respect to $[Ce^{4+}]$).

Although Ce^{4+} diffusivity should have a strong dependence on Ce^{4+} and Ce^{3+} concentrations, a constant diffusivity D is assumed in the model based on two approximations: (1) the diffusion of Ce^{4+} or Ce^{3+} in the MOF channel is fast compared to the experimental time scale so that the sum of $[Ce^{4+}] + [Ce^{3+}]$ within the MOF, especially in the outer-shell that can be reached by Ce^{4+} (see below), quickly reaches the same level of the bulk solution at the very beginning of the experimental measurement; (2) Ce^{4+} and Ce^{3+}, due to the similarity of their chemical structures, have a similar concentration effect on the diffusivity of Ce^{4+}, so that the Ce^{4+} diffusivity only depends on the sum of $[Ce^{4+}] + [Ce^{3+}]$, which is constant throughout the course of reaction.

The first approximation can be validated by calculating a characteristic diffusional time of Ce^{4+}, $t_D = (\%d_{0.01}a)^2/D$, where $\%d_{0.01}$ is the depth of the outer shell of a MOF particle that can be reached by Ce^{4+} with concentration >1% of that in the solution (see eq S36, SI, for details) and comparing it to the experimental time scale. As listed in Tables S3 and S4, SI, all of these characteristic diffusional times (0.03−0.18 min for **1** and 0.004−0.014 min for **2**) were significantly smaller than the experimental time scale (>1 min), indicating that the $[Ce^{4+}]$ +

$[Ce^{3+}]$ concentration quickly reached the level in the bulk solution at the very beginning of the experiments.

To validate the second approximation of a similar influence of $[Ce^{3+}]$ and $[Ce^{4+}]$ on the diffusivity of Ce^{4+}, we carried out WORs with **1** by adding a mixture of Ce^{3+} and Ce^{4+} to the catalyst. As shown in Figures 9a and S43, SI, with different initial Ce^{4+} concentrations (C_0) but the same total Ce concentration ($[Ce^{3+}] + [Ce^{4+}]$), the $[Ce^{4+}]/C_0$ curves nearly overlap with each other, indicating that Ce^{4+} exhibits similar diffusivity in **1** under these conditions. Moreover, the kinetic data with different initial Ce^{3+} and Ce^{4+} concentrations were fitted to the reaction−diffusion model to obtain Ce^{4+} diffusivities. As shown in Figure S56, SI, the dependence of Ce^{4+} diffusivities on the sums of $[Ce^{3+}] + [Ce^{4+}]$ only slightly deviates from the dependence of Ce^{4+} diffusivities on the $[Ce^{4+}]$ when pure Ce^{4+} was added to the catalyst at the beginning. These results indicate that there is a only slight difference of the dependence of Ce^{4+} diffusivity on $[Ce^{4+}]$ and $[Ce^{3+}]$, thus validating our approximation of a similar influence of $[Ce^{3+}]$ and $[Ce^{4+}]$ on the diffusivity of Ce^{4+}. Ce^{4+} can be transported into the MOF interior via the Ce^{4+}/Ce^{3+} self-exchange in addition to the direct diffusion of Ce^{4+} through the channels. However, the negligible dependence of Ce^{4+} diffusivity on Ce^{3+}/Ce^{4+} ratios indicates that the self-exchange pathway is not significant in these reactions.

The reaction rate law of a single catalyst site in the MOF can be estimated from kinetic measurements of homogeneous catalysts. The reaction rate dependence of HOMO-**1** (see scheme 1) on $[Ce^{4+}]$ was reported to be of the 0.7th order.[6b] Our own measurements also confirmed that the rate dependence slightly deviates from the first order, which is presumably due to the decomposition of the WOC during the course of the reaction. To account for less decomposition of the WOC in the MOF and to simplify mathematical derivations, we approximated the rate dependence to be first order and determined a rate constant of 100 $min^{-1}\cdot mM^{-1}$ using HOMO-**1** (Section S6.1, SI). A similar approximation was applied to HOMO-**2** with a rate constant of 200 $min^{-1}\cdot mM^{-1}$ (Section S6.1, SI). HOMO-**2** was chosen as the homogeneous model because the aromatic amine is protonated at pH = 1 to increase the catalyst solubility in water.

Equation 1 was solved by Laplace transformation under the boundary conditions of eqs 2 and 3 (See Section S7, SI for detailed approximations and mathematical derivations).[27] The obtained infinite summation solution was simplified by approximating an elliptic θ function to a simpler piecewise function (eq S15, SI).

Assuming the $[Ce^{4+}]$ in the bulk solution C_s (which can be detected by UV−vis measurements) equals the $[Ce^{4+}]$ on the MOF surface, eq 4 was then obtained, which describes the quasi-first-order kinetic behavior for the **2**-catalyzed reaction. The amount of Ce^{4+} inside the MOF at a given time was insignificant (<0.0043%) compared to the amount in the solution and can be ignored in the C_s quantification.

$$\frac{d \ln\left(\frac{c_s}{c_0}\right)}{dt} = -\beta \cdot \frac{\sqrt{kD}}{a}\left(1 - \frac{1}{a}\sqrt{\frac{D}{k}}\right) \tag{4}$$

Here β is defined as $(N\cdot 4\pi a^3)/V$. For **1**, however, a further linearization approximation can be made (eq S30, SI), leading to a quasi-zeroth-order reaction described by

$$\frac{d\frac{c_s}{c_0}}{dt} = -\beta \cdot \frac{\sqrt{kD}}{a}\left(1 - \frac{1}{a}\sqrt{\frac{D}{k}}\right) \tag{5}$$

This linearization approximation will only hold when $\beta \frac{\sqrt{kD}}{a}\left(1 - \frac{1}{a}\sqrt{\frac{D}{k}}\right)t \ll 1$. The validity of this assumption for **1** but not for **2** can be verified by calculating a characteristic time $t_a = \frac{1}{\beta \frac{\sqrt{kD}}{a}\left(1 - \frac{1}{a}\sqrt{\frac{D}{k}}\right)}$. Only when $t_a \gg t$, the approximation holds. As shown in Tables S4 and S5, SI, $t_a \gg t$ holds for **1** (120−670 min) but does not hold for **2** (12−55 min). This difference in t_a explains different kinetic behaviors of the two MOFs.

By fitting the experimental data to these equations, the Ce^{4+} diffusivity values were obtained (Table 2). As expected, the

Table 2. Diffusivities of Ce^{4+} at Different Initial $[Ce^{4+}]$'s in 1 and 2

1		2	
c_0 (mM)	D (/10^{-11} cm^2 s^{-1})	c_0 (mM)	D (/10^{-11} cm^2 s^{-1})
0.29	1.52	0.11	67.9
0.98	0.221	0.30	38.8
2.03	0.099	0.40	41.0
2.88	0.053	0.51	4.6
4.61	0.050	0.61	4.1
5.69	0.046	1.09	3.4
6.97	0.046		

Ce^{4+} diffusivities determined from these analyses are highly dependent on the Ce concentration: the lower the concentration, the higher the diffusivity. Ce^{4+} diffusivities in **2** are significantly larger than those in **1**, consistent with the expectation that positively charged species should diffuse faster through neutral channels in **2** than through positively charged channels in **1**.

As the experimental time scale is significantly larger than the characteristic diffusional time $t_D = a^2/D$, the reaction−diffusion process inside these MOFs are at the steady state. With the kinetic model, the Ce^{4+} distributions inside the MOFs at the steady state can be calculated, using the following equation (eqs S33−S35, SI):

$$\frac{c}{c_s} = \frac{a}{r}\cdot \frac{\sinh\left(\sqrt{\frac{k}{D}}r\right)}{\sinh\left(\sqrt{\frac{k}{D}}a\right)} \tag{6}$$

The $[Ce^{4+}]$ inside the MOF relative to that in the solution C/C_s at the steady state with a total Ce concentration of 1 mM is plotted in Figure 9b. Because of the fast reaction rate and relatively slow diffusion rate, the Ce^{4+} can only diffuse into the particle of **1** at ~11% in depth (30% in volume for a spherical object) before being consumed for the WOR to form Ce^{3+} (with $[Ce^{4+}] < 1\%$ C_s). As the diffusion of Ce^{4+} in **2** is much faster, Ce^{4+} can diffuse deeper inside the particle (27% in depth and 61% in volume) before being reduced to Ce^{3+}.

The uneven distribution of Ce^{4+} inside the MOF particle in this reaction−diffusion model perfectly explains the fact that the original Cp*Ir catalysts were still observed from digested samples of the recovered **1** in spite of extensive oxidative degradation of the Cp* rings. Based on this reaction−diffusion model, the outer shell of the MOF particles can be oxidatively

modified, while the interior of the MOF particle is seldom reached by Ce^{4+} and remains intact. As a result, both the original unmodified and the oxidatively modified complexes were observed in the digested samples of the recovered **1**.

3. CONCLUSIONS

We have constructed two porous and stable Zr-carboxylate MOFs (**1** and **2**) with elongated bpy- or ppy-containing dicarboxylate ligands (**bpy-dc** and **ppy-dc**) attached to the Cp*Ir moieties and studied their water oxidation activities. As a result of site isolation in the crystalline frameworks, these MOFs provided an interesting platform to study water oxidation pathways owing to the elimination of multimolecular degradation pathways. Oxidative modification of the Cp* rings of the immobilized Ir complexes was observed with Ce^{4+} as an oxidant. Careful studies of the recovered **1** from WORs revealed the identity of (**bpy-dc**)$Ir(H_2O)_2XCl$ (X is likely a formate or acetate group) as an active catalyst for water oxidation, which was supported by XPS, UV−vis, luminescence, and infrared spectroscopies as well as detailed kinetic studies of Ce^{4+}-driven WORs. Although our experimental data suggest but cannot unambiguously confirm the role of the original catalyst L_1 itself as an active WOC, the modified (**bpy-dc**)$Ir(H_2O)_2XCl$ species resulted from the oxidative degradation of Cp* groups must be an active WOC to account for water oxidation activity of the reused MOFs. A reaction−diffusion model was developed to describe the kinetics of the MOF-catalyzed WORs, revealing an intricate balance between reaction and diffusion rates that account for the partial oxidative degradation of L_1 to form (**bpy-dc**)$Ir(H_2O)_2XCl$. This work not only highlights the importance of studying water oxidation pathways in organized assemblies that more closely resemble the WOCs in functional devices but also presents a general strategy of using MOFs to study catalytic mechanisms of molecular species by taking advantage of site isolation in MOF structures and the ease of isolating solid materials from reaction mixtures for further spectroscopic and other characterization.

■ ASSOCIATED CONTENT

Ⓢ Supporting Information

Detailed experimental procedures, including general procedures, synthesis and characterization of ligands and MOFs, water oxidation studies, spectroscopic information, kinetic studies, and kinetic modeling. This material is available free of charge via the Internet at http://pubs.acs.org.

■ AUTHOR INFORMATION

Corresponding Author
*wlin@unc.edu

Author Contributions
[†]These authors contributed equally.

Notes
The authors declare no competing financial interest.

■ ACKNOWLEDGMENTS

■ REFERENCES

(1) (a) Gust, D.; Moore, T. A.; Moore, A. L. *Acc. Chem. Res.* **2009**, *42*, 1890. (b) Barber, J. *Chem. Soc. Rev.* **2009**, *38*, 185.

(2) (a) Ohno, T.; Bai, L.; Hisatomi, T.; Maeda, K.; Domen, K. *J. Am. Chem. Soc.* **2012**, *134*, 8254. (b) Zhang, F.; Yamakata, A.; Maeda, K.; Moriya, Y.; Takata, T.; Kubota, J.; Teshima, K.; Oishi, S.; Domen, K. *J. Am. Chem. Soc.* **2012**, *134*, 8348. (c) Reece, S. Y.; Hamel, J. A.; Sung, K.; Jarvi, T. D.; Esswein, A. J.; Pijpers, J. J. H.; Nocera, D. G. *Science* **2011**, *334*, 645. (e) Nakagawa, T.; Bjorge, N. S.; Murray, R. W. *J. Am. Chem. Soc.* **2009**, *131*, 15578. (f) Youngblood, W. J.; Lee, S. H. A.; Kobayashi, Y.; Hernandez-Pagan, E. A.; Hoertz, P. G.; Moore, T. A.; Moore, A. L.; Gust, D.; Mallouk, T. E. *J. Am. Chem. Soc.* **2009**, *131*, 926. (g) Zhao, Y.; Swierk, J. R.; Megiatto, J. D.; Sherman, B.; Youngblood, W. J.; Qin, D.; Lentz, D. M.; Moore, A. L.; Moore, T. A.; Gust, D.; Mallouk, T. E. *Proc. Nat. Aca. Sci.* **2012**, *109*, 15612. (d) Jiao, F.; Frei, H. *Angew. Chem., Int. Ed. Engl.* **2009**, *48*, 1841.

(3) (a) Moyer, B. A.; Meyer, T. J. *Inorg. Chem.* **1981**, *20*, 436. (b) Gersten, S. W.; Samuels, G. J.; Meyer, T. J. *J. Am. Chem. Soc.* **1982**, *104*, 4029.

(4) (a) Concepcion, J. J.; Jurss, J. W.; Templeton, J. L.; Meyer, T. J. *J. Am. Chem. Soc.* **2008**, *130*, 16462. (b) Concepcion, J. J.; Tsai, M.-K.; Muckerman, J. T.; Meyer, T. J. *J. Am. Chem. Soc.* **2010**, *132*, 1545. (c) Dismukes, G. C.; Brimblecombe, R.; Felton, G. A. N.; Pryadun, R. S.; Sheats, J. E.; Spiccia, L.; Swiegers, G. F. *Acc. Chem. Res.* **2009**, *42*, 1935. (d) Fillol, J. L.; Codolà, Z.; Garcia-Bosch, I.; Gómez, L.; Pla, J. J.; Costas, M. *Nat. Chem.* **2011**, *3*, 807. (e) Wasylenko, D. J.; Ganesamoorthy, C.; Borau-Garcia, J.; Berlinguette, C. P. *Chem. Commun.* **2011**, *47*, 4249. (f) Barnett, S. M.; Goldberg, K. I.; Mayer, J. M. *Nat. Chem.* **2012**, *4*, 498. (g) Duan, L.; Bozoglian, F.; Mandal, S.; Stewart, B.; Privalov, T.; Llobet, A.; Sun, L. *Nat. Chem.* **2012**, *4*, 418. (h) Kärkäs, M. D.; Åkermark, T.; Johnston, E. V.; Karim, S. R.; Laine, T. M.; Lee, B.-L.; Åkermark, T.; Privalov, T.; Åkermark, B. *Angew. Chem., Int. Ed. Engl.* **2012**, *51*, 11589. (i) Yin, Q.; Tan, J. M.; Besson, C.; Geletii, Y. V.; Musaev, D. G.; Kuznetsov, A. E.; Luo, Z.; Hardcastle, K. L.; Hill, C. L. *Science* **2010**, *328*, 5976. (j) Lv, H.; Geletii, Y. V.; Zhao, C.; Vickers, J. W.; Zhu, G.; Luo, Z.; Song, J.; Lian, T.; Musaev, D. G.; Hill, C. L. *Chem. Soc. Rev.* **2012**, *41*, 7572.

(5) (a) McCool, N. S.; Robinson, D. M.; Sheats, J. E.; Dismukes, G. C. *J. Am. Chem. Soc.* **2011**, *133*, 11446. (b) Ellis, W. C.; McDaniel, N. D.; Bernhard, S.; Collins, T. J. *J. Am. Chem. Soc.* **2010**, *132*, 10990. (c) McDaniel, N. D.; Coughlin, F. J.; Tinker, L. L.; Bernhard, S. *J. Am. Chem. Soc.* **2007**, *130*, 210.

(6) (a) Hull, J. F.; Balcells, D.; Blakemore, J. D.; Incarvito, C. D.; Eisenstein, O.; Brudvig, G. W.; Crabtree, R. H. *J. Am. Chem. Soc.* **2009**, *131*, 8730. (b) Blakemore, J. D.; Schley, N. D.; Balcells, D.; Hull, J. F.; Olack, G. W.; Incarvito, C. D.; Eisenstein, O.; Brudvig, G. W.; Crabtree, R. H. *J. Am. Chem. Soc.* **2010**, *132*, 16017.

(7) (a) Blakemore, J. D.; Schley, N. D.; Olack, G. W.; Incarvito, C. D.; Brudvig, G. W.; Crabtree, R. H. *Chem. Sci.* **2011**, *2*, 94. (b) Grotjahn, D. B.; Brown, D. B.; Martin, J. K.; Marelius, D. C.; Abadjian, M. C.; Tran, H. N.; Kalyuzhny, G.; Vecchio, K. S.; Specht, Z. G.; Cortes-Llamas, S. A.; Miranda-Soto, V.; van Niekerk, C.; Moore, C. E.; Rheingold, A. L. *J. Am. Chem. Soc.* **2011**, *133*, 19024. (c) Savini, A.; Belanzoni, P.; Bellachioma, G.; Zuccaccia, C.; Zuccaccia, D.; Macchioni, A. *Green Chem.* **2011**, *13*, 3360.

(8) (a) Hara, M.; Mallouk, T. E. *Chem. Commun.* **2000**, 1903. (b) Hara, M.; Lean, J. T.; Mallouk, T. E. *Chem. Mater.* **2001**, *13*, 4668.

(9) Hintermair, U.; Hashmi, S. M.; Elimelech, M.; Crabtree, R. H. *J. Am. Chem. Soc.* **2012**, *134*, 9785.

(10) Schley, N. D.; Blakemore, J. D.; Subbaiyan, N. K.; Incarvito, C. D.; D'Souza, F.; Crabtree, R. H.; Brudvig, G. W. *J. Am. Chem. Soc.* **2011**, *133*, 10473.

(11) (a) Parent, A. R.; Blakemore, J. D.; Brudvig, G. W.; Crabtree, R. H. *Chem. Commun.* **2011**, *47*, 11745. (b) Parent, A. R.; Brewster, T. P.; De Wolf, W.; Crabtree, R. H.; Brudvig, G. W. *Inorg. Chem.* **2012**, *51*, 6147.

(12) Zuccaccia, C.; Bellachioma, G.; Bolano, S.; Rocchigiani, L.; Savini, A.; Macchioni, A. *Eur. J. Inorg. Chem.* **2012**, 1462.

(13) Hong, D. C.; Murakami, M.; Yamada, Y.; Fukuzumi, S. *Energy Environ. Sci.* **2012**, *5*, 5708.

(14) (a) deKrafft, K. E.; Wang, C.; Xie, Z. G.; Su, X.; Hinds, B. J.; Lin, W. B. *ACS Appl. Mater. Interfaces* **2012**, *4*, 608. (b) Joya, K. S.; Subbaiyan, N. K.; D'Souza, F.; de Groot, H. J. M. *Angew. Chem., Int. Ed. Engl.* **2012**, *51*, 9601.

(15) (a) Evans, O. R.; Lin, W. *Acc. Chem. Res.* **2002**, *35*, 511. (b) Eddaoudi, M.; Kim, J.; Rosi, N.; Vodak, D.; Wachter, J.; O'Keeffe, M.; Yaghi, O. M. *Science* **2002**, *295*, 469. (c) Sumida, K.; Rogow, D. L.; Mason, J. A.; McDonald, T. M.; Bloch, E. D.; Herm, Z. R; Bae, T. H.; Long, J. R. *Chem. Rev.* **2012**, *112*, 724. (d) Seo, J. S.; Whang, D.; Lee, H.; Jun, S. I.; Oh, J.; Jeon, Y. J.; Kim, K. *Nature* **2000**, *404*, 982. (e) Wu, C. D.; Hu, A.; Zhang, L.; Lin, W. *J. Am. Chem. Soc.* **2005**, *127*, 8940. (f) Ma, L.; Falkowski, J. M.; Abney, C.; Lin, W. *Nat. Chem.* **2010**, *2*, 838. (g) Song, F.; Wang, C.; Falkowski, J. M.; Ma, L.; Lin, W. *J. Am. Chem. Soc.* **2010**, *132*, 15390. (h) Lin, W.; Rieter, W. J.; Taylor, K. M. *Angew. Chem., Int. Ed. Engl.* **2009**, *48*, 650. (i) Della Rocca, J.; Lin, W. B. *Eur. J. Inorg. Chem.* **2010**, 3725. (j) Rieter, W. J.; Pott, K. M.; Taylor, K. M.; Lin, W. *J. Am. Chem. Soc.* **2008**, *130*, 11584. (k) Taylor-Pashow, K. M. L.; Della Rocca, J.; Huxford, R. C.; Lin, W. B. *Chem. Commun.* **2010**, *46*, 5832.

(16) Lan, A.; Li, K.; Wu, H.; Olson, D. H.; Emge, T. J.; Ki, W.; Hong, M.; Li, J. *Angew. Chem., Int. Ed. Engl.* **2009**, *48*, 2334.

(17) Kent, C. A.; Mehl, B. P.; Ma, L.; Papanikolas, J. M.; Meyer, T. J.; Lin, W. *J. Am. Chem. Soc.* **2010**, *132*, 12767.

(18) (a) Ma, L.; Abney, C.; Lin, W. *Chem. Soc. Rev.* **2009**, *38*, 1248. (b) Lee, J.; Farha, O. K.; Roberts, J.; Scheidt, K. A.; Nguyen, S. T.; Hupp, J. T. *Chem. Soc. Rev.* **2009**, *38*, 1450. (c) Yoon, M.; Srirambalaji, R.; Kim, K. *Chem. Rev.* **2011**, *112*, 1196.

(19) Cho, S.-H.; Ma, B.; Nguyen, S. T.; Hupp, J. T.; Albrecht-Schmitt, T. E. *Chem. Comm* **2006**, 2563.

(20) Zhang, T.; Song, F.; Lin, W. *Chem. Comm* **2012**, *48*, 8766.

(21) Zheng, M.; Liu, Y.; Wang, C.; Liu, S.; Lin, W. *Chem. Sci* **2012**, *3*, 2623.

(22) (a) Wang, C.; Xie, Z. G.; deKrafft, K. E.; Lin, W. L. *J. Am. Chem. Soc.* **2011**, *133*, 13445. (b) Cavka, J. H.; Jakobsen, S.; Olsbye, U.; Guillou, N.; Lamberti, C.; Bordiga, S.; Lillerud, K. P. *J. Am. Chem. Soc.* **2008**, *130*, 13850.

(23) Wang, C.; deKrafft, K. E.; Lin, W. *J. Am. Chem. Soc.* **2012**, *134*, 7211.

(24) Ma, L.; Jin, A.; Xie, Z.; Lin, W. *Angew. Chem., Int. Ed. Engl.* **2009**, *48*, 9905.

(25) (a) Serre, C.; Millange, F.; Thouvenot, C.; Noguès, M.; Marsolier, G.; Louër, D.; Férey, G. *J. Am. Chem. Soc.* **2002**, *124*, 13519. (b) Llewellyn, P. L.; Maurin, G.; Devic, T.; Loera-Serna, S.; Rosenbach, N.; Serre, C.; Bourrelly, S.; Horcajada, P.; Filinchuk, Y.; Férey, G. *J. Am. Chem. Soc.* **2008**, *130*, 12808.

(26) (a) Schmeier, T. J.; Dobereiner, G. E.; Crabtree, R. H.; Hazari, N. *J. Am. Chem. Soc.* **2011**, *133*, 9274. (b) Deeming, A. J.; Proud, G. P. *J. Organomet. Chem.* **1986**, *301*, 385. (c) Curtis, N. J.; Sargeson, A. M. *J. Am. Chem. Soc.* **1984**, *106*, 625.

(27) Crank, J. *The Mathematics of Diffusion*, 2nd ed.; Oxford University Press: Oxford, U.K., 1975.